Letters in Applied NanoBioScience
Open-Access Journal (ISSN: 2284-6808)

Article
Volume 15, **Issue 2**, **2026**, **56**
https://doi.org/10.33263/LIANBS152.056

Exploring Calcium and Copper Metals in Nanohybrid Synthesis for Enhanced Chlorophyllin Immobilization: Targeting Extensively Drug-resistant *Pseudomonas aeruginosa* PAW1 through Photokilling

Suneha Shukla [1,2], Manisha Shinde [2], Akshada Jagtap [2], Vishakha Surve [2], Sunil Bhapkar [2], Shweta Jagtap [3], Sandeep Pai [4], Garima Gupta [1,*], Karishma Pardesi [2], Madhumita Tawre [2], Gajanan Ghodake [5], Umesh Jadhav [2,*]

[1] Faculty of Biosciences, Institute of Biosciences and Technology, Shri Ramswaroop Memorial University, Lucknow-Dewa Road, Barabanki, Uttar Pradesh, India
[2] Department of Microbiology, Savitribai Phule Pune University, Pune, Maharashtra, India
[3] Department of Instrumentation Science, Savitribai Phule Pune University, Pune, Maharashtra, India
[4] Department of Botany, Rayat Shikshan Sanstha's Dada Patil Mahavidyalaya, Karjat, Maharashtra, India
[5] Department of Biological and Environmental Science, Dongguk University-Seoul, 32 Dongguk-ro, Ilsandong-gu, Goyang-si 10326, Gyeonggi-do, Republic of Korea
* Correspondence: garimagupta.ibst@srmu.ac.in (G.G.); ujadhav@unipune.ac.in (U.J.);
Received: 25.07.2025; Accepted: 28.02.2026; Published: 30.06.2026

Abstract: This study investigates chlorophyllin as a natural photosensitizer for photodynamic inactivation of extensively drug-resistant (EDR) Pseudomonas aeruginosa PAW1. Chlorophyllin was incorporated into copper- and calcium-based organic–inorganic nanohybrids, and copper phosphate emerged as the preferred host due to its stable flower-like morphology. The Chlorophyllin-$Cu_3(PO_4)_2$ nanohybrid retained the photoactivity of chlorophyllin and achieved complete bacterial inactivation under visible light. Mechanistic analysis indicates that the antimicrobial activity is predominantly mediated by light-induced reactive oxygen species that compromise cell membrane integrity. Control experiments confirmed negligible dark toxicity and minimal contribution from metal-ion release, supporting a primarily photokilling mechanism. These results highlight the promise of Chlorophyllin-$Cu_3(PO_4)_2$ nanohybrids as photoactive antimicrobial materials against the EDR bacterium.

Keywords: *Pseudomonas aeruginosa* PAW1; extensively drug resistant; chlorophyllin; nanohybrid; photokilling.

1. Introduction

The global rise of antimicrobial resistance (AMR), driven by the overuse of antibiotics, has rendered many conventional therapies ineffective, particularly against ESKAPE (*Enterococcus faecium*, *Staphylococcus aureus*, *Klebsiella pneumoniae*, *Acinetobacter baumannii*, *Pseudomonas aeruginosa*, and *Enterobacter* spp) pathogens [1]. Among these, *Pseudomonas aeruginosa* is listed by the World Health Organization (WHO) as a critical priority pathogen due to its multidrug resistance and persistence in hospital environments [2,3]. This growing resistance necessitates the development of alternative antimicrobial strategies beyond conventional antibiotics.

Photodynamic therapy (PDT) has emerged as a promising non-antibiotic approach for pathogen inactivation [1]. In PDT, a photosensitizer (PS) generates reactive oxygen species (ROS) upon light activation, leading to oxidative damage and bacterial death [4]. However, most PSs are hydrophobic, prone to aggregation and photodegradation, and often inactivated by plasma components, limiting their biomedical use [5]. Encapsulation within nanoscale carriers can improve PS stability and delivery [6,7]. Although polymeric micelles, liposomes, and metal nanoparticles have been explored as PS carriers, many suffer from low encapsulation efficiency, limited reusability, and environmentally harsh synthesis routes [8].

To address these challenges, the present study utilizes nanohybrid/nanoflower structures to encapsulate the natural photosensitizer chlorophyllin. Nanohybrids are a newly developed class of tiny particles. They show structural similarity to plant flowers [9]. The formation of organic-inorganic hybrid nanoflowers typically proceeds through a three-step process involving nucleation, growth, and completion [10]. In the nucleation stage, divalent metal ions coordinate with functional groups of the organic component, such as amide, carboxyl, or hydroxyl moieties, initiating the formation of primary metal phosphate nanocrystals.

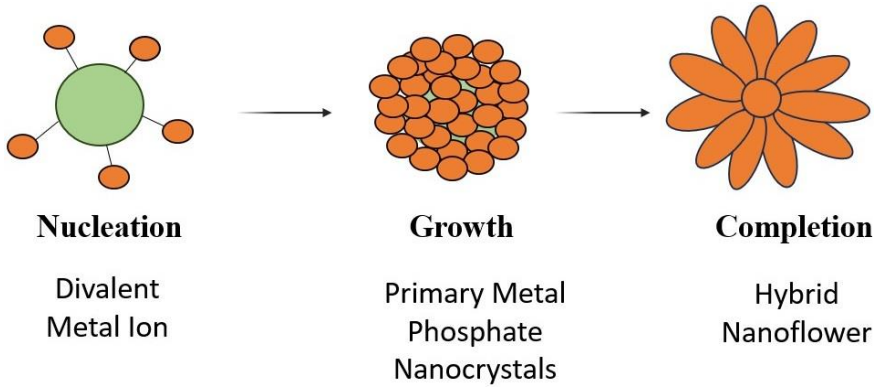

Figure 1. Mechanism of nanohybrid synthesis.

During the growth stage, these primary crystals interact with organic molecules to form aggregated hybrid structures, and anisotropic crystal growth begins to produce petal-like morphologies. In the final completion stage, prolonged incubation promotes the self-assembly and consolidation of these petals into well-defined flower-shaped microstructures (Figure 1). The cooperative interactions between divalent metal ions and organic ligands govern the directionality of crystal growth, ultimately yielding micrometer-sized hybrid particles composed of nanoscale petal architectures with high surface area and structural stability [11]. Increasing interest in these types of nanohybrids is being paid due to their simple preparation method, non-toxicity, and cost-effectiveness [12]. They can be synthesized from organic, inorganic, or a combination of both materials. They integrate the functional versatility of organic molecules with the physicochemical stability of inorganic phases. Their flower-like architecture provides an exceptionally large surface area, enhanced mass transfer, and abundant active sites, making them highly attractive for catalytic, sensing, environmental, and biomedical applications [10]. The morphology and functionality of these materials are strongly influenced by the nature of the metal ions and their coordination behavior with the organic counterpart. Several divalent metal ions-including Cu^{2+}, Ca^{2+}, Zn^{2+}, Mn^{2+}, Co^{2+}, and Ni^{2+}-have been reported for the fabrication of hybrid nanoflowers, each imparting distinct structural and functional attributes depending on ionic radius, bonding strength, and nucleation kinetics [11,13,14].

In the present study, copper(II) and calcium(II) ions were selected as comparative systems to investigate how metal-ligand coordination influences the formation of chlorophyllin-based nanohybrids. Copper(II), a transition metal with a $3d^9$ electronic configuration, readily forms strong Cu–N/O coordination bonds with the porphyrin-like chlorophyllin structure, thereby facilitating controlled nucleation and anisotropic crystal growth. This tendency toward coordination often leads to the formation of hierarchical "flower-like" nanostructures with enhanced photoactive and antimicrobial properties, making Cu-based hybrids attractive for biomedical applications [10]. In contrast, calcium(II), an abundant and biogenic element, primarily exhibits ionic Ca-O interactions with weaker coordination, resulting in less anisotropic, more compact morphologies suitable for biocompatible and food-grade applications [11].

Comparative synthesis using both metal systems enabled evaluation of the role of coordination chemistry in nanoflower formation. Among them, copper-based nanohybrids exhibited a distinct flower-like morphology and superior structural stability; therefore, they were selected for detailed characterization and assessment of photokilling performance against extensively drug-resistant (*EDR*) *Pseudomonas aeruginosa* PAW1, in comparison with free chlorophyllin.

2. Materials and Methods

2.1. Materials.

Copper sulfate ($CuSO_4$) (Sigma-Aldrich, Catalog No. 7758-98-7), chlorophyllin sodium copper salt, and the chemicals for preparation of Phosphate Buffered Saline (PBS) were commercially obtained from Sigma-Aldrich (Sigma-Aldrich, Catalog No. 8048-12-6). The Luria Bertani (LB) broth and Mueller-Hinton agar for bacterial growth and sub-culturing were procured from Hi-Media Laboratories (Hi-Media, Catalog No. M001; Cat No. M173).

2.2. Synthesis of Chlorophyllin-$Cu_3(PO_4)_2$ and Chlorophyllin-$Ca_3(PO_4)_2$ nanohybrid.

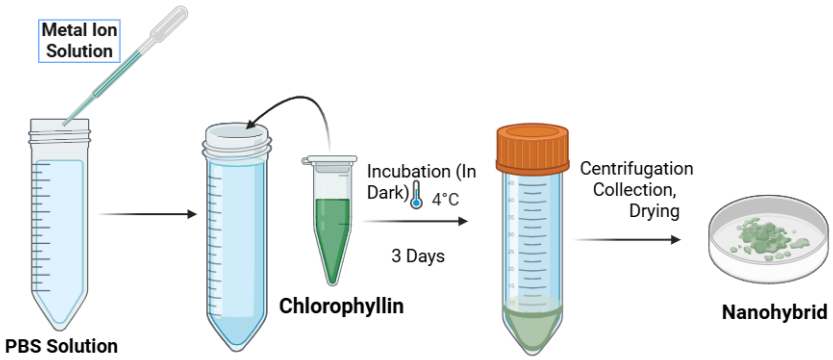

Figure 2. Schematics showing Chlorophyllin-metal $(PO_4)_2$ nanohybrid synthesis process.

A sodium salt of chlorophyllin was used for nanohybrid synthesis. The nanohybrid with and without chlorophyllin was synthesized by adopting a previously optimized process [15]. For the synthesis of Chlorophyllin-$Cu_3(PO_4)_2$ nanohybrid, typically, 0.2 ml of chlorophyllin solution was added to 50 mL of 10 mM PBS (pH 7.4). Then 1 ml of $CuSO_4$ (200 mM) was added. The solution was vortexed for 30 s. Then it was incubated at 4°C in the dark for 3 days under static conditions in the refrigerator. The precipitate that occurred at the bottom of the reaction tubes was collected by centrifugation (Kubota cooling centrifuge 6500) at 10,000 rpm

for 15 min. The precipitate was washed thrice with PBS buffer. The final product was dried at 4°C in the dark to get nanohybrid powder (Figure 2). The synthesis of the nanohybrid without chlorophyllin was carried out by mixing 50 mL PBS (10 mM, pH 7.4) with 1 mL of $CuSO_4$ (200 mM). In this reaction mixture, chlorophyllin solution was not added.

For the synthesis of Chlorophyllin-$Ca_3(PO_4)_2$ nanohybrid, typically, 0.2 ml of chlorophyllin solution was added to 50 mL of 10 mM PBS (pH 7.4). Then 1 mL of $CaCl_2$ (200 mM) was added (Figure 1). The synthesis of the nanohybrid without chlorophyllin was carried out by mixing 50 mL PBS (10 mM, pH 7.4) with 1 mL of $CaCl_2$ (200 mM). In this reaction mixture, chlorophyllin solution was not added.

2.3. Characterization of Chlorophyllin-$Cu_3(PO_4)_2$.

The Chlorophyllin-$Cu_3(PO_4)_2$ and Chlorophyllin-$Ca_3(PO_4)_2$ nanohybrid were characterized using Scanning Electron Microscopy (SEM) (FEI Nova NanoSEM 450, Resolution 1 nm at 15 KV and 30 pa) from the central instrumentation facility, Savitribai Phule Pune University. Fourier Transform Infrared Spectroscopy (FT-IR, Burker Platinum Tensor 37) was used to analyze Chlorophyllin-$Cu_3(PO_4)_2$ [15,16] in Pune, Maharashtra, India. The Chlorophyllin-$Cu_3(PO_4)_2$ and Chlorophyllin-$Ca_3(PO_4)_2$ nanohybrid were analyzed using hydrodynamic radius (DLS), and zeta potential measurements were performed using a NanoBrook Omni-Brookhaven particle size and zeta potential analyzer with a 1 cm x 1 cm plastic cuvette. The Panalytical Empyrean-4 was used for X-ray diffraction (XRD) analysis.

2.4. Determination of chlorophyllin encapsulation efficiency.

The ability of Chlorophyllin-$Cu_3(PO_4)_2$ nanohybrid to encapsulate chlorophyllin at varying concentrations (5-30 mM) was studied by separately adding chlorophyllin solutions of the respective concentrations to a mixture containing PBS and $CuSO_4$. The precipitate was removed by centrifugation, and the chlorophyllin concentration in the supernatant was measured by recording the absorbance at 406 nm using a spectrophotometer (Shimadzu UV-1800 spectrophotometer). The chlorophyllin encapsulation (%) was determined by finding the ratio of the amount of chlorophyllin immobilized to the total amount of chlorophyllin used. The percent encapsulation efficiency was calculated by using the following formula as described by Yu *et al*. [17]:

$$\%Encapsulation = \frac{Initial\ OD - Final\ OD}{Initial\ OD} X\ 100 \qquad 1$$

2.5. Photodynamic antimicrobial activity.

The antibacterial activity of Chlorophyllin-$Cu_3(PO_4)_2$ nanohybrid was determined against *P. aeruginosa* PAW1. The *P. aeruginosa* PAW1 culture was pre-grown in Luria Bertani (LB) broth at 37°C overnight. The culture broth containing *P. aeruginosa* PAW1 was then centrifuged at 5000 rpm for 15 min. The pellet was resuspended in sterile saline, and the optical density (OD_{600}) was adjusted to 0.1. Then, 900 µL of microbial culture (containing *P. aeruginosa* cells at an OD_{600} of 0.1) was mixed with Chlorophyllin-$Cu_3(PO_4)_2$ nanohybrid (10 mg). The photokilling activity was initiated by exposing this mixture (kept in a transparent glass bottle) to a light source (having a wavelength in the visible range). The light source was kept at a distance of 4.5 cm from the sample. After the light exposure, the mixture was serially diluted using sterile saline. An appropriate dilution was selected, and 10 µL of microbial culture

from this dilution was spread on the Mueller-Hinton agar plate. Further plates were incubated at 30°C for 24 h to determine the CFU. A similar antibacterial activity experiment was conducted by mixing 900 µL of a microbial culture (containing a fixed number of cells) with chlorophyllin solution and exposing the mixture to the light source.

The impact of light exposure time on the photokilling of *P. aeruginosa* PAW1 was studied. It was carried out for varying durations (5-20 min). The rest of the process was the same as described in the previous section. Similarly, the effect of Chlorophyllin-$Cu_3(PO_4)_2$ nanohybrid on photokilling of *P. aeruginosa* PAW1 was studied. A varying amount of Chlorophyllin-$Cu_3(PO_4)_2$ nanohybrid powder (5-15 mg) was used during this experiment. Appropriate controls, such as free chlorophyllin (under dark conditions), the chlorophyllin-$Cu_3(PO_4)_2$ nanohybrid (under dark conditions), $Cu_3(PO_4)_2$ alone (under illuminated light and dark conditions), were tested to assess bactericidal levels of chlorophyllin (dark toxicity) and of copper ions.

The *P. aeruginosa* PAW1 membrane integrity after light exposure was checked as described by Buchovec *et al*. [18]. The supernatant was collected after the photodynamic antibacterial activity experiment, and its absorbance was monitored at λ260 nm (DNA absorption peak) and λ280 nm (protein absorption peak).

2.6. DPBF singlet-oxygen ($^1O_2$) generation assay.

An experiment was carried out to identify the generation of $^1O_2$ during photokilling, using a protocol described by Attaoui *et al*. [19]. Singlet-oxygen production was quantified via the decay of DPBF absorbance at 410 nm. DPBF (50 µM final) was prepared in ethanol: PBS (10:90 v/v) and incubated with photosensitizer samples (free chlorophyllin, Cu-nanohybrids) in quartz cuvettes (2.0 mL). Samples were irradiated with the same light source used during the photokilling experiment, and A_{410} was recorded after 30 min and 60 min. Controls included DPBF + light (no PS), DPBF + PS (dark). The percentage DPBF remaining was calculated using the following formula,

$$\%A(t) = \frac{A(t)}{A(0)} X100 \qquad 2$$

Where
A(t)= absorbance at time t
A(0)= absorbance at time 0

2.7. Statistical analysis.

Tukey method was implemented to evaluate statistical differences in encapsulation efficiency determination and antimicrobial activity experiments at $p \leq 0.05$ using GraphPad Prism 8.4.3 (686 version). All assays were performed in triplicate (n=3), and the data were visualized as mean with standard deviation.

3. Results and Discussion

3.1. Synthesis of nanohybrid.

The present study reports the immobilization of the natural photosensitizer chlorophyllin in the form of a nanohybrid. The nanohybrid can be synthesized from organic, inorganic materials, or a combination of both [12]. The organic components typically refer to molecules that contain carbon atoms bonded to hydrogen, oxygen, and nitrogen. The inorganic

components refer to various metals [20]. Most of the studies have reported the use of copper for nanohybrid synthesis [21]. However, Ca^{2+}, Zn^{2+}, Co^{2+}, Mn^{2+}, Fe^{2+}, and Mg^{2+} were also used for the immobilization of organic constituents in the form of a nanohybrid [22-27]. The interaction between the organic component and the metal ions is the primary driving force for nanohybrid formation. Also, the type of metal ions plays an important role in the formation of nanohybrids [21].

Therefore, in the present study, chlorophyllin immobilization was carried out and compared using copper and calcium. The initial absorbance of chlorophyllin + PBS buffer was 1.135 (au) at 406 nm. The appearance of small crystals immediately after mixing the metal solution, chlorophyllin, and PBS buffer indicated the nanohybrid synthesis (Figure 2).

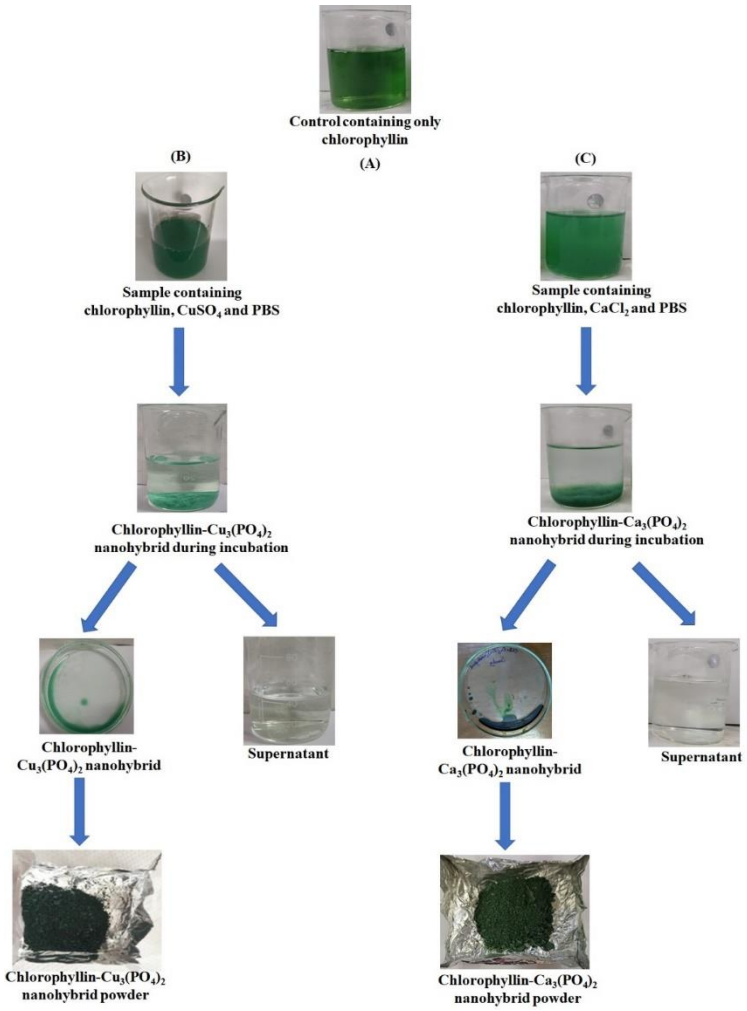

Figure 3. Experimental setup showing various stages of nanohybrid synthesis **(A)** Control containing chlorophyllin + PBS; **(B)** Chlorophyllin is mixed with $CuSO_4$ and PBS buffer to get Chlorophyllin-$Cu_3(PO_4)_2$ powder; **(C)** Chlorophyllin is mixed with $CaCl_2$ and PBS buffer to get Chlorophyllin-$Ca_3(PO_4)_2$.

During 3 days of incubation, the respective nanohybrid precipitate was formed and settled at the bottom of the container. The precipitate was separated by centrifugation and kept for drying at 4°C. The visual observation of samples indicates the disappearance of chlorophyllin color from the reaction mixture (Figure 3). The absorbance of supernatant separated after removal of Chlorophyllin-$Cu_3(PO_4)_2$ and Chlorophyllin-$Ca_3(PO_4)_2$ precipitate was 0.085 and 0.097 (au), respectively (data not shown). These results suggest that the chlorophyllin is immobilized in a nanohybrid. The organic-inorganic nanohybrids undergo molecular self-assembly during their synthesis [28]. The interaction between the hydrophobic

and hydrophilic residues of the organic component and the metal-phosphate affects the morphological and physicochemical properties of the hybrids [29].

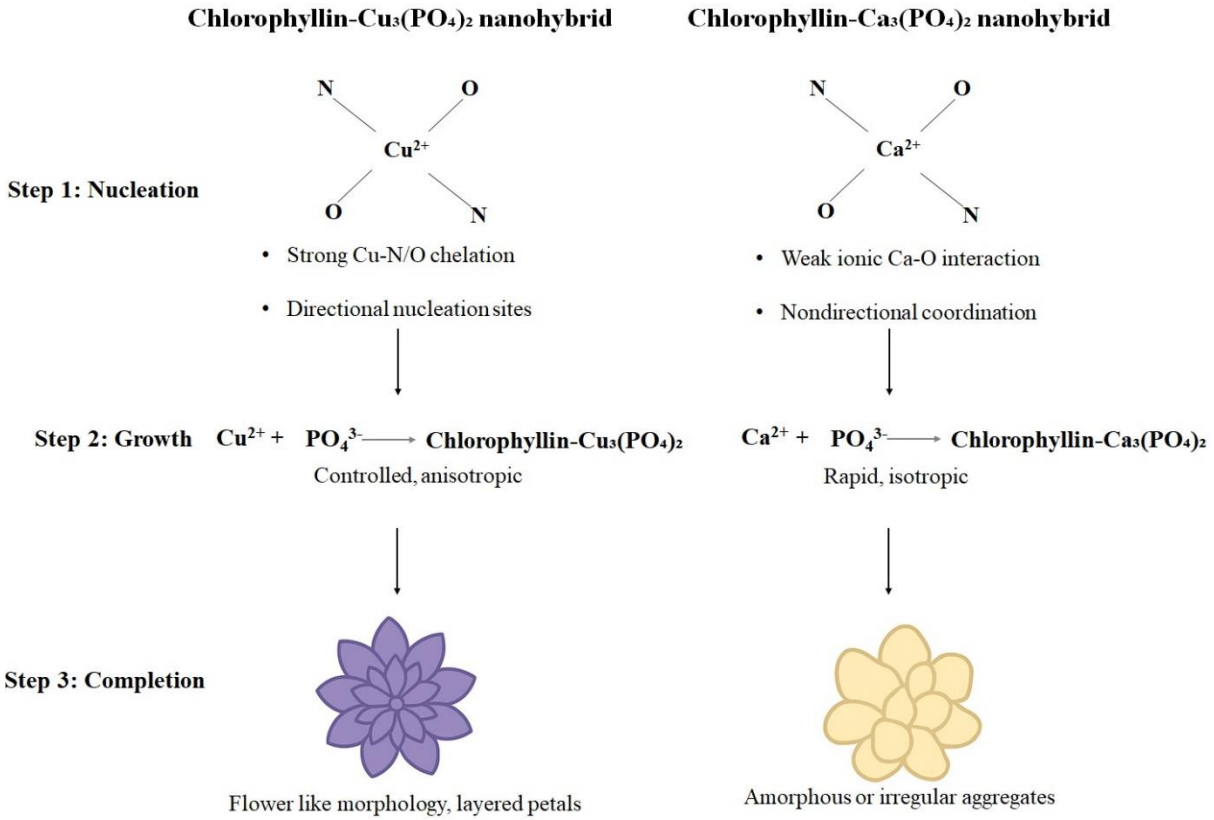

Figure 4. Schematic illustration showing the difference in coordination chemistry and morphological evolution between Cu^{2+}– and Ca^{2+}–chlorophyllin nanohybrid systems.

The nanohybrid formation process starts with the binding of biomolecules with metal ions in the presence of phosphate buffer. This leads to the formation of nucleation sites (Figure 3). These nucleation sites provide space for the growth of metal phosphate, generating the flower-like structure [30]. However, the different groups present in biomolecules exert different affinities for various metals [31]. In the Cu^{2+} system (Figure 4 left), the transition metal ion coordinates with both nitrogen and oxygen donor atoms of the chlorophyllin macrocycle, forming mixed Cu-N and Cu-O bonds that act as strong and directional nucleation sites. The resulting Chlorophyllin-$Cu_3(PO_4)_2$ complexes facilitate slow and anisotropic growth of $Cu_3(PO_4)_2$ petals, yielding well-defined flower-like architectures. In contrast, Ca^{2+} (Figure 4 right) primarily forms weak, ionic interactions with carboxylate oxygen atoms of chlorophyllin, resulting in the Chlorophyllin-$Ca_3(PO_4)_2$ complex. The absence of ligand field stabilization and directional bonding leads to rapid, isotropic precipitation of $Ca_3(PO_4)_2$, producing amorphous or aggregated morphologies. This comparative behavior supports the mechanistic model described by Lee *et al.* [10], indicating that transition-metal coordination strength and ligand-field effects govern the hierarchical assembly of organic-inorganic hybrid nanoflowers. This hypothesis was further supported by SEM analysis, revealing intriguing morphological differences between Chlorophyllin-$Cu_3(PO_4)_2$ and Chlorophyllin-$Ca_3(PO_4)_2$ nanohybrids. Notably, while the interaction between Chlorophyllin and $Ca_3(PO_4)_2$ did occur, the expected flower-like morphology was absent. In stark contrast, the interaction with $Cu_3(PO_4)_2$ produced a remarkable flower-like nanohybrid morphology (Figure 5).

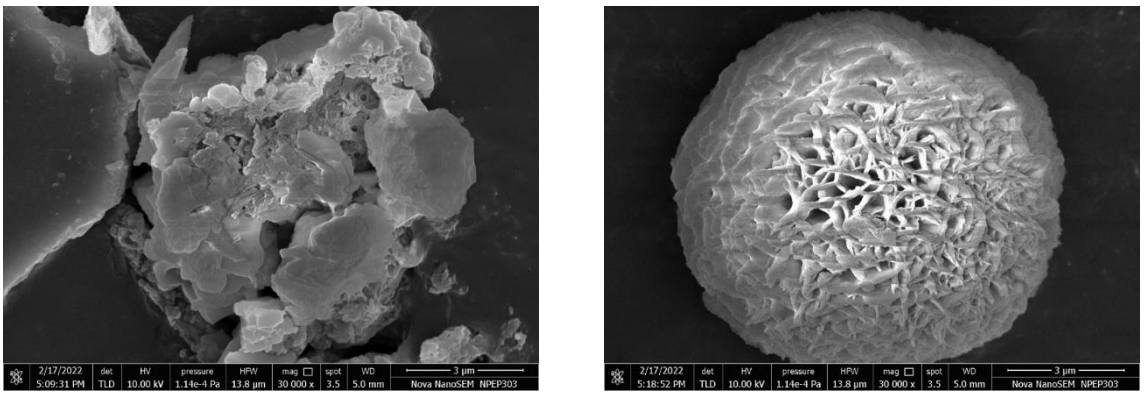

(a) **(b)**

Figure 5 SEM micrographs captured at 30000 x magnification and 3 µm scale showing the morphology of synthesized nanohybrid **(a)** irregular shape of Chlorophyllin-$Ca_3(PO_4)_2$; **(b)** flower mimicking Chlorophyllin-$Cu_3(PO_4)_2$.

Escobar *et al*. [32] showed the formation of lipase nanohybrid with different shapes by using various metal ions. Similarly, the chlorophyllin showed varying affinity towards Cu and Ca ions. This is evident from SEM micrographs showing different morphologies that were obtained for Chlorophyllin-$Cu_3(PO_4)_2$ and Chlorophyllin-$Ca_3(PO_4)_2$ nanohybrids (Figure 5). Additionally, the encapsulation efficiency of chlorophyllin was studied. Notably, chlorophyllin encapsulation of 92% for copper and 91% for calcium was observed (data not shown). The Chlorophyllin-$Cu_3(PO_4)_2$ nanohybrid was selected for further studies because of its distinct flower-like morphology.

The FTIR spectrum of the divalent-metal-organic hybrid nanoflower (Figure 6) shows characteristic vibrational features arising from both the organic moiety and the metal-phosphate inorganic phase.

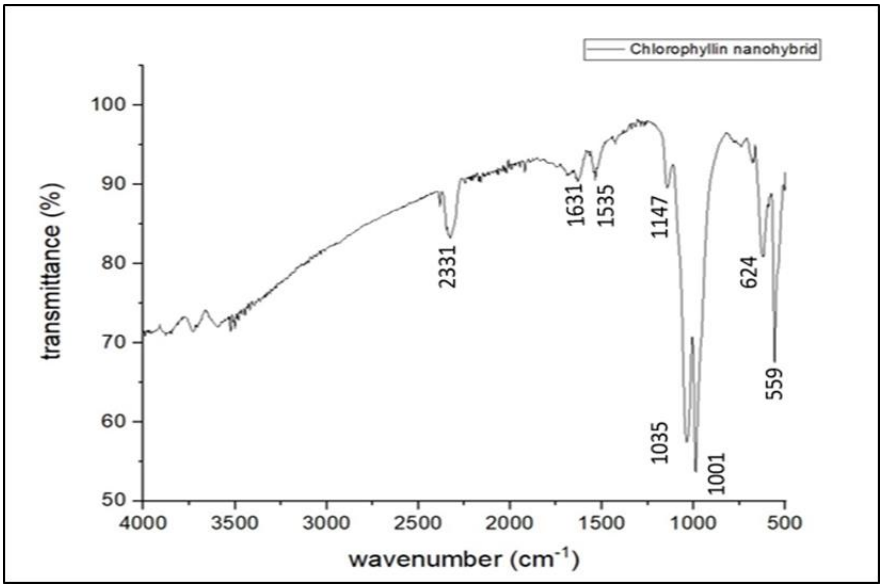

Figure 6. FTIR spectra of as-synthesized Chlorophyllin-$Cu_3(PO_4)_2$ nanohybrid.

A broad band centered around 1000-1150 cm^{-1} (observed at 1001 and 1148 cm^{-1}) corresponds to overlapping C-O stretching vibrations and PO_4^{3-}-related symmetric/asymmetric stretching modes. Phosphate ν_1 and ν_3 vibrations are widely reported in this spectral window for metal phosphates, with their exact positions dependent on crystal structure and metal coordination [11,13]. The peak at ~1035 cm^{-1} aligns with pyrrole/porphyrin ring in-plane breathing modes typical of chlorophyllin-like macrocycles, consistent with the established porphyrin vibrational assignments reported in classical spectroscopic references [33,34]. Low-

frequency bands at ~559 cm^{-1} and ~625 cm^{-1} are attributed to metal–oxygen (M-O) lattice vibrations, consistent with reported FTIR signatures of copper-containing oxides and copper-phosphate materials, which typically exhibit strong M-O stretching features in the 450-700 cm^{-1} region [10]. These bands persist only in the nanohybrid and inorganic reference spectra, supporting the presence of a metal–oxygen–phosphate framework. A band at 1535 cm^{-1} is attributed to N-H bending coupled with C-N stretching (amide II region), commonly observed in organic ligands containing amide, pyrrole, or substituted nitrogen functionalities [33]. The band near 1631 cm^{-1} in the spectrum of the free organic component corresponds to H-bonded O-H bending or C=O/C=C stretching, a region characteristic of conjugated and hydrogen-bonded chromophores. The peak at 2331 cm^{-1} shows the C-N triple bond stretch [35,36]. Overall, the persistence of metal–oxygen and phosphate stretching features alongside organic macrocycle vibrations confirms the successful immobilization of the organic component within a divalent-metal phosphate matrix, consistent with the formation of the intended hybrid nanoflower structure.

Dynamic light scattering (DLS) analysis showed that the chlorophyllin-$Cu_3(PO_4)_2$ nanohybrids formed microscale aggregates with an average hydrodynamic diameter of 13.29 ± 0.42 µm, whereas the $Cu_3(PO_4)_2$ nanohybrids synthesized without chlorophyllin were slightly larger, measuring 18.37 ± 0.14 µm. This reduction in particle diameter upon chlorophyllin incorporation suggests that the pigment participates in nucleation and slows uncontrolled inorganic growth, leading to the formation of more compact hybrid structures. The zeta potentials of both formulations were moderately negative [–21.89 ± 0.16 mV for chlorophyllin–$Cu_3(PO_4)_2$; –22.61 ± 1.06 mV for $Cu_3(PO_4)_2$] (Table 1), indicating comparable surface charge characteristics dominated by exposed phosphate groups and deprotonated functional moieties. These values suggest sufficient colloidal electrostatic stability for aqueous dispersions of the micron-sized hybrid aggregates. The formation of micron-scale hybrid particles in the present study is consistent with previous nanoflower research, in which hierarchical petal-like architectures frequently fall within the 5-50 µm range. Nadar *et al*. [37] reported glucoamylase–$Cu_3(PO_4)_2$ nanoflowers with typical diameters of 10-20 µm, attributed to enzyme-mediated directional growth of $Cu_3(PO_4)_2$ petals into large, flower-like aggregates. The hydrodynamic sizes measured in our study (13-18 µm) fall squarely within this range, suggesting that chlorophyllin-Cu^{2+}-phosphate coordination yields analogous self-assembled architectures despite the smaller molecular size and planar structure of chlorophyllin relative to bulky protein scaffolds. However, the slight size reduction observed for chlorophyllin-loaded nanohybrids compared with bare $Cu_3(PO_4)_2$ hybrids indicates that chlorophyllin modulates early nucleation dynamics by binding to Cu^{2+} ions and limiting excessive, anisotropic growth. This is consistent with reports that small organic ligands, such as porphyrins, riboflavin derivatives, or polyphenols, can template hybrid nanoflower formation by regulating growth kinetics. Studies by Wang *et al*. [9] and Hu *et al*. [13] similarly show that organic molecules lacking tertiary protein structure often form smaller, denser nanoflowers compared with enzyme-templated assemblies, because of their more restricted steric footprint and weaker ability to propagate petal extension.

Table 1. Dynamic light scattering (DLS) size and zeta potential of chlorophyllin–$Cu_3(PO_4)_2$ nanohybrids and $Cu_3(PO_4)_2$ nanohybrids (Values represent mean ± standard deviation [n = 3]).

Analysis	Chlorophyllin-$Ca_3(PO_4)_2$ nanohybrids	$Ca_3(PO_4)_2$ nanohybrids
Zeta potential	-21.89 ± 0.16	-22.61 ± 1.06
Size measured using DLS (um)	13.29 ± 0.42	18.37 ± 0.14

The negative zeta potentials (–21 to –23 mV) (Table 1) observed here are also in agreement with Nadar *et al*., who reported moderately negative surface charges for $Cu_3(PO_4)_2$ nanoflowers, reflecting the abundance of exposed phosphate groups at the particle surface. The similarity in zeta potential between chlorophyllin-containing and chlorophyllin-free hybrids suggests that chlorophyllin is incorporated predominantly inside or between petals rather than forming a dominant surface coating. This is again consistent with the more compact architecture and smaller hydrodynamic diameter recorded for the hybrid system.

Overall, the DLS and zeta potential data demonstrate that chlorophyllin actively participates in the self-assembly of $Cu_3(PO_4)_2$ nanohybrids, producing micron-sized, moderately stable particles comparable to previously published organic–inorganic nanoflowers but with a somewhat reduced size profile relative to enzyme-based systems. These physicochemical properties are expected to influence the photodynamic and antimicrobial performance of the nanohybrids by affecting surface area, porosity, and chlorophyllin distribution within the hybrid structure.

Figure 7 presents the comparative XRD patterns of pure $Cu_3(PO_4)_2$ and the Chlorophyllin–$Cu_3(PO_4)_2$ hybrid. Both samples exhibited a series of sharp, intense peaks characteristic of crystalline copper(II) phosphate, in agreement with the standard JCPDS reference data reported in earlier organic-inorganic hybrid nanoflower studies [21,37].

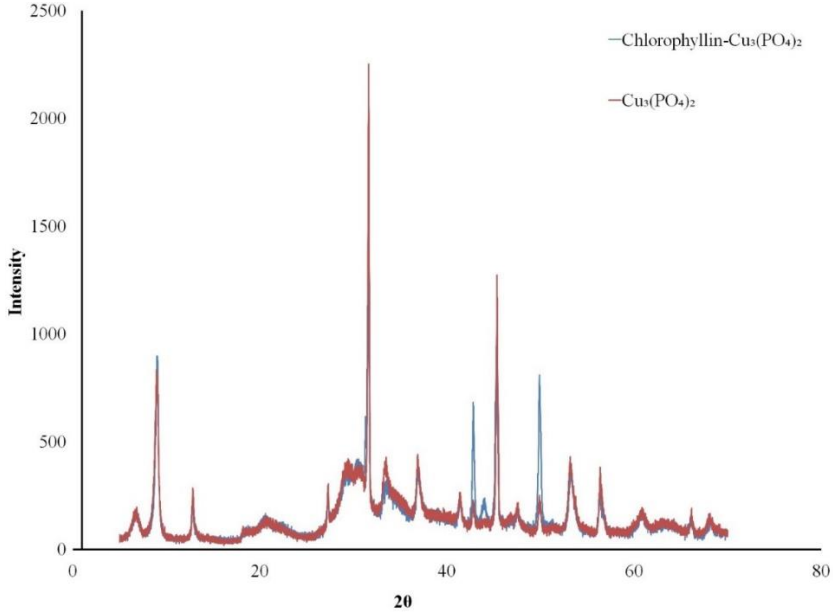

Figure 7. Comparative XRD profiles of $Cu_3(PO_4)_2$ and Chlorophyllin–$Cu_3(PO_4)_2$. The characteristic reflections of $Cu_3(PO_4)_2 \cdot 3H_2O$ are observed in both materials, whereas the hybrid exhibits slight peak broadening and intensity variation due to organic–inorganic interactions during hybrid formation. No additional crystalline phases were detected.

The diffraction profiles of the two materials displayed identical peak positions, confirming that the inorganic $Cu_3(PO_4)_2$ lattice is structurally preserved during the synthesis process. This observation is consistent with previous reports on enzyme-$Cu_3(PO_4)_2$ nanoflowers, in which the biomolecular component supports the nucleation and growth of copper phosphate without altering its crystallographic identity [15-17,21,37]. Although the peak positions in the hybrid remain unchanged, the relative intensities of several reflections show notable differences compared with $Cu_3(PO_4)_2$. In particular, the major reflections in the Chlorophyllin-$Cu_3(PO_4)_2$ pattern exhibit moderate broadening and reduced intensity, which may arise from a combination of (i) decreased crystallite size, (ii) increased lattice disorder, and (iii) partial coverage of copper phosphate by the amorphous chlorophyllin matrix. These

effects are widely reported in enzyme-$Cu_3(PO_4)_2$ hybrids, where incorporation of a non-crystalline organic component disrupts long-range order but does not produce new crystallographic phases [17,37]. Importantly, no additional diffraction peaks corresponding to copper oxide (CuO, Cu_2O), metallic copper, or other impurity phases were observed in either sample, indicating that the synthesis conditions yield phase-pure $Cu_3(PO_4)_2$ and that the interaction with chlorophyllin does not induce secondary crystallization or decomposition pathways. The absence of new reflections further confirms that chlorophyllin remains amorphous within the nanohybrid structure, a common feature shared with biological macromolecules in enzyme-inorganic nanoflowers. Overall, the XRD results demonstrate that the Chlorophyllin-$Cu_3(PO_4)_2$ hybrid retains the crystalline backbone of $Cu_3(PO_4)_2$ while exhibiting structural modifications at the nanoscale, consistent with the formation of an organic-inorganic hybrid framework. These findings strongly support the proposed flower-like assembly mechanism and corroborate the morphological features observed in SEM micrographs.

3.2. Encapsulation efficiency.

The encapsulation efficiency of chlorophyllin in Chlorophyllin-$Cu_3(PO_4)_2$ was determined using the spectrophotometric method. The encapsulation efficiency increased with the chlorophyllin concentration, rising from 75% at 5 mM to 92% at 20 mM. However, the encapsulation efficiency decreased when the chlorophyllin concentration was increased to 25 and 30 mM. Therefore, a concentration of 20 mM chlorophyllin was found to be optimal for synthesizing Chlorophyllin-$Cu_3(PO_4)_2$ with an encapsulation efficiency of 92% (Figure 8). A similar increase in the encapsulation efficiency of α-chymotrypsin was reported by Yin *et al.* [38].

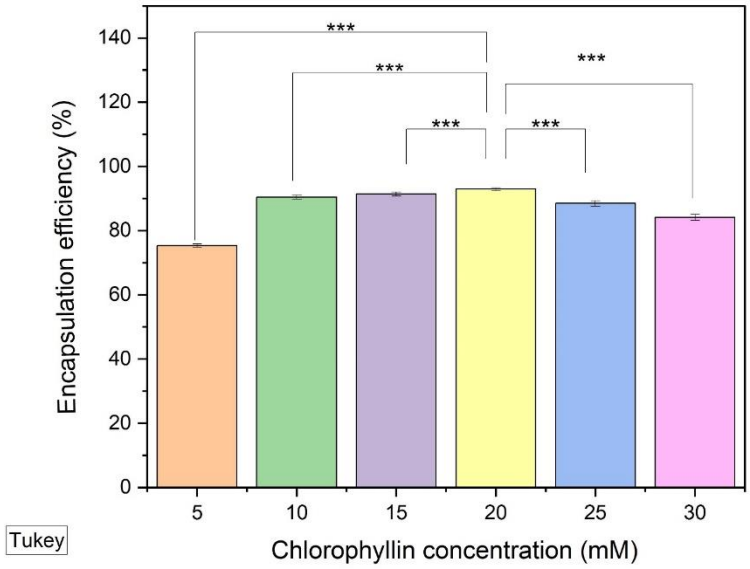

Figure 8. Encapsulation efficiency of varying chlorophyllin concentrations (5-30 mM) in chlorophyllin-$Cu_3(PO_4)_2$ nanohybrid. The values represent the mean of ratios ± SD (n=3), and the values are significantly different at ($p \leq 0.05$).

The decline in encapsulation efficiency beyond a 20 mM chlorophyllin concentration might be due to the reduced availability of copper ions. The synthesis process of the nanohybrid depends on the interaction between the organic component (chlorophyllin) and the inorganic component (copper phosphate) [37]. In the present study, chlorophyllin molecules provided binding sites on their surfaces for the attachment of copper in PBS, leading to self-assembly

into a specific pattern or structure. According to Jiang *et al*. [39], increasing the concentration of organic molecules could reduce the number of copper ions available to coordinate with organic molecules. Thus, increasing the chlorophyllin concentration beyond 20 mM adversely affected the encapsulation efficiency.

3.3. Photokilling of P. aeruginosa PAW1 using Chlorophyllin-$Cu_3(PO_4)_2$.

The photokilling of drug-resistant *P. aeruginosa* PAW1 using a chlorophyllin solution and Chlorophyllin-$Cu_3(PO_4)_2$ nanohybrid demonstrated remarkable antibacterial efficacy. Through direct contact testing, the control group, devoid of both the nanohybrid and light exposure, maintained 116 (±0.75) CFU (Figure 9a). Astonishingly, *P. aeruginosa* PAW1 cells subjected to Chlorophyllin-$Cu_3(PO_4)_2$ nanohybrid under light exposure showed a complete eradication (0 CFU) (Figure 9b).

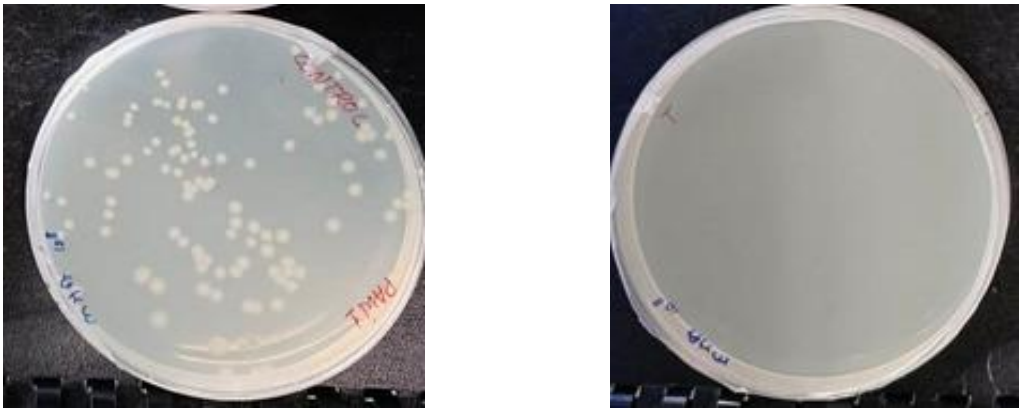

(a) **(b)**

Figure 9. Growth of *P. aeruginosa* PAW1 **(a)** control group, devoid of both the nanohybrid and light exposure; **(b)** after exposure to chlorophyllin-$Cu_3(PO_4)_2$ nanohybrid (10 mg) and light source (2100 Lumen) for 20 min at a distance of 4.5 cm from the sample.

To distinguish pure photokilling effects from possible dark toxicity or copper-ion-mediated antibacterial action, a photokilling experiment was performed with appropriate controls. As shown in Table 2, neither free chlorophyllin nor the chlorophyllin-$Cu_3(PO_4)_2$ nanohybrid exhibited any appreciable dark toxicity, with CFU values (112 ± 0.02 and 109 ± 0.08, respectively) comparable to the untreated control (116 ± 0.75). Similarly, $Cu_3(PO_4)_2$ alone showed negligible antibacterial activity under both dark (106 ± 0.30) and illuminated (108 ± 0.15) conditions, indicating that copper phosphate does not release bactericidal levels of copper ions under the experimental conditions. In contrast, illumination in the presence of either free chlorophyllin or the chlorophyllin-$Cu_3(PO_4)_2$ nanohybrid resulted in complete bacterial inactivation (0 CFU), confirming that the antibacterial effect arises exclusively from the photokilling process. These results demonstrate that the observed killing is light-dependent, photosensitizer-specific, and not attributable to dark toxicity, passive copper ion release, or $Cu_3(PO_4)_2$ itself.

Table 2. Photokilling of *P. aeruginosa* PAW1 under different conditions (Comparison of colony-forming units [CFU/mL] after treatment with free chlorophyllin or chlorophyllin–$Cu_3(PO_4)_2$ nanohybrids under illuminated and dark conditions. Light-activated samples show pronounced CFU reduction, confirming photokilling, while dark controls exhibit minimal changes. Values are presented as mean ± standard deviation [n = 3].

Experimental condition	CFU
Control	116 (±0.75)
Chlorophyllin (light)	0

Experimental condition	CFU
Chlorophyllin (dark)	112 (±0.02)
Chlorophyllin-$Cu_3(PO_4)_2$ (light)	0
Chlorophyllin-$Cu_3(PO_4)_2$ (dark)	109 (±0.08)
$Cu_3(PO_4)_2$ (light)	108 (±0.15)
$Cu_3(PO_4)_2$ (dark)	106 (±0.30)

Several studies have suggested that photosensitizers are less effective against Gram-negative bacteria than against Gram-positive bacteria [40-42]. According to these studies, the cell wall of Gram-negative bacteria is more complex than that of Gram-positive bacteria. It has a negatively charged outer membrane. These properties of Gram-negative bacteria interfere with their interaction with the photosensitizer, resulting in lower generation of reactive oxygen species around the bacterium and thus less harm to the cell [40]. However, in the present study, no such effect was observed. The Chlorophyllin-$Cu_3(PO_4)_2$ nanohybrid effectively killed *P. aeruginosa* PAW1 cells in 20 minutes of exposure time. These findings underscore the powerful photokilling capability of the Chlorophyllin-$Cu_3(PO_4)_2$ nanohybrid, defying the commonly held notion that photosensitizers are less effective against Gram-negative bacteria. Unlike previous studies [40-42], our study demonstrates that the encapsulation of chlorophyllin in the nanohybrid facilitates sufficient ROS generation to effectively kill *P. aeruginosa* PAW1. The results of the DPBF decay experiment also overrule the necessity of the intake of photosensitizers by bacterial cells. The ROS generated outside the bacterial cell by Chlorophyllin-$Cu_3(PO_4)_2$ nanohybrid can effectively damage the bacterial cells. A study by Buchovec *et al*. [18] reported a similar phenomenon of immobilizing chlorophyllin on chitosan polymer for the inactivation of the Gram-negative food pathogen *Salmonella enterica*.

Another experiment was carried out to study the light exposure duration on the photokilling of *P. aeruginosa* PAW1. The CFU percentage reduction of *P. aeruginosa* PAW1cells increased with an increase in exposure time from 5 min to 20 min. The 5 min exposure of *P. aeruginosa* PAW1 cells to Chlorophyllin-$Cu_3(PO_4)_2$ nanohybrid and light resulted in 83.44 (±0.21) CFU percentage reduction.

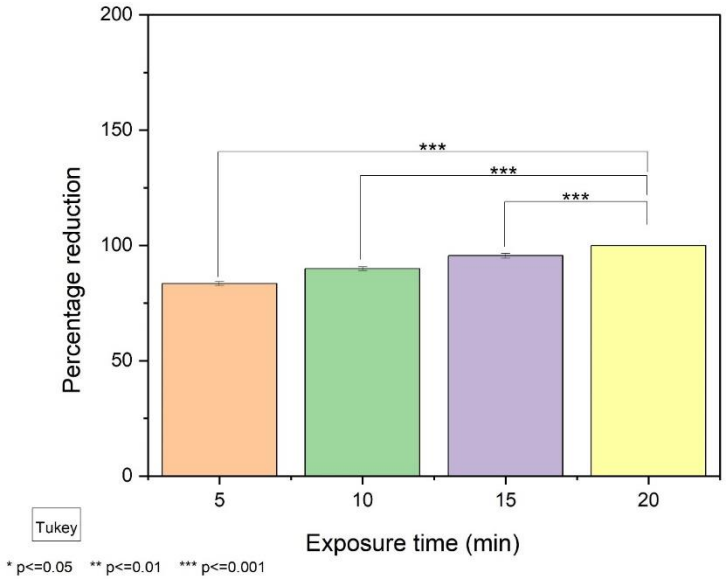

Figure 10. Effect of varying light exposure time (5-20 min) on growth of *P. aeruginosa* PAW1 in the presence of chlorophyllin-$Cu_3(PO_4)_2$ nanohybrid (10 mg). The values represent the mean of ratios ± SD (n=3), and the values are significantly different at ($p \leq 0.05$).

The increase in exposure time to 10 and 15 min showed 89.9 (±0.32) and 95.56 (±0.67) CFU percentage reduction, respectively. The 100% CFU percentage reduction was observed

when *P. aeruginosa* PAW1 cells were exposed to Chlorophyllin-$Cu_3(PO_4)_2$ nanohybrid and light for 20 min (Fig. 10). This efficiency surpasses previous findings [43], which required longer incubation times to kill *E. coli* cells using chlorophyllin solution. Additionally, varying the amount of Chlorophyllin-$Cu_3(PO_4)_2$ nanohybrid powder confirmed that 10 mg was sufficient for complete bacterial eradication (data not shown). These compelling results suggest that Chlorophyllin-$Cu_3(PO_4)_2$ nanohybrid is a potent photoactive antibacterial agent, with significant potential for applications in drug-resistant bacterial inactivation. When the Chlorophyllin-$Cu_3(PO_4)_2$ nanohybrid is exposed to light, the chlorophyllin encapsulated into the nanohybrid becomes reactive. Due to exposure of chlorophyllin to light, the energy associated with the light radiation is transferred to an electron of chlorophyllin. The electron goes to an excited state from the ground state. After this, it follows a Type II photochemical reaction.

The excited state electron loses its energy, which is transferred to molecular oxygen. This results in the formation of reactive oxygen species (ROS) and singlet oxygen ($^1O_2$) [44]. When bacterial cells come in contact with such ROS and $^1O_2$, it results in cell damage on various levels, such as membranes, proteins, and DNA, leading to cell death [45]. There are discrepancies in the requirement for the generation of extracellular or intracellular ROS for the effective photokilling of bacteria [46,47]. However, few studies suggested that the uptake of a photosensitizer is not always necessary to inactivate bacteria [46,47]. The present study showed that chlorophyllin doesn't need to enter the bacterial cells.

To further prove sufficient ROS generation during photokilling, an experiment was carried out. Singlet oxygen ($^1O_2$) generation by free chlorophyllin and the chlorophyllin-$Cu_3(PO_4)_2$ nanohybrid was evaluated using the DPBF photodegradation assay. Control samples showed minimal DPBF decay in the dark (96-97% remaining), confirming negligible background photooxidation. Under identical illumination, free chlorophyllin induced more rapid DPBF decay, with 30 ± 1.9% DPBF remaining at 30 min and 12 ± 1.5% at 60 min, consistent with efficient $^1O_2$ generation (Table 3). The chlorophyllin-$Cu_3(PO_4)_2$ nanohybrid displayed a slower DPBF decay (retaining 39 ± 2.0% at 30 min and 17 ± 0.9% at 60 min). These observations are supported by prior reports that chlorophyllin derivatives/sodium chlorophyllin photosensitizers can produce rapid DPBF photodegradation under irradiation [48,49]. The moderate reduction in bulk $^1O_2$ yield for the nanohybrid can be explained by well-known photophysical effects of immobilization [19]. Taken together, our DPBF results show that both free chlorophyllin and the chlorophyllin-$Cu_3(PO_4)_2$ nanohybrid are photoactive and capable of generating singlet oxygen. Importantly, the nanohybrid produces effective photokilling.

Table 3. Singlet oxygen generation assessed by DPBF photodegradation under illuminated and dark conditions. (Percentage of DPBF absorbance remaining [A_{410}] after exposure to light for 30 and 60 minutes in the presence of free chlorophyllin, chlorophyllin–$Cu_3(PO_4)_2$ nanohybrids, and corresponding dark controls. Lower DPBF percentages under illumination indicate greater singlet oxygen production, while minimal decay in the dark confirms the light-dependent nature of ROS generation. Values represent mean ± standard deviation [n = 3].

Time (min)	DPBF decay percent (%) of initial A_{410} remaining					
	DPBF only (light)	DPBF only (dark)	DPBF + chlorophyllin (light)	DPBF + chlorophyllin (dark)	DPBF + chlorophyllin-$Cu_3(PO_4)_2$ (light)	DPBF + chlorophyllin-$Cu_3(PO_4)_2$ (dark)
30	90 ± 1.0	97 ± 0.8	30 ± 1.9	96 ± 0.6	39 ± 2.0	97 ± 0.4
60	87 ± 0.7	96 ± 0.8	12 ± 1.5	93 ± 0.5	17 ± 0.9	95 ± 0.7

The chlorophyllin encapsulated in Chlorophyllin-$Cu_3(PO_4)_2$ nanohybrid was able to show cytotoxic effects against *P. aeruginosa* PAW1. This effect was further analyzed by checking bacterial membrane integrity after light exposure. The control *P. aeruginosa* PAW1 cells showed negligible release of intracellular components absorbing at λ260 nm (DNA absorption peak) and λ280 nm (protein absorption peak). The absorbance of the control supernatant at λ260 nm and λ280 nm was 0.010 and 0.009, respectively. However, it increased when *P. aeruginosa* PAW1 cells were exposed to a light source and Chlorophyllin-$Cu_3(PO_4)_2$ nanohybrid. The supernatant of treated cells showed absorbance of 1.05 and 0.98 at λ260 nm and λ280 nm, respectively (data not shown). These results confirm the breakdown of the *P. aeruginosa* PAW1 cell membrane. It is not possible for *P. aeruginosa* PAW1 cells to generate resistance against photokilling since the cell integrity is being compromised. Buchovec *et al*. [18] observed a similar phenomenon of leakage of intracellular components of *S. enterica* after treating the cells with photoactivated Chl–CHS complex for 60 min. These results also rule out the requirement of proximity of chlorophyllin to the cells (e.g., to bind to the cell membrane) as suggested by Krüger *et al*. [46].

The photokilling performance observed in this study is consistent with earlier reports demonstrating the broad antimicrobial potential of chlorophyllin-based PDT systems. Arifianto *et al*. [50] showed that chlorophyllin and curcumin enhance photodynamic inactivation of *Aggregatibacter actinomycetemcomitans* and *Enterococcus faecalis*, achieving multi-log reductions under LED irradiation - values comparable to or slightly higher than our free-chlorophyllin treatment, depending on PS dose and irradiation parameters. Similarly, Wimmer *et al*. [51] reported effective inactivation of *Candidozyma auris* planktonic cells and biofilms using chlorophyllin, highlighting its potency even against highly stress-resistant fungal pathogens. Vourvoutsiotou *et al*. [52] demonstrated clear dose- and time-dependent killing of *Bacillus subtilis*, again reinforcing that chlorophyllin is a reliable broad-spectrum photosensitizer whose performance strongly depends on formulation, fluence rate, and PS concentration. Comparisons can also be drawn with hybrid or nanocarrier-based PDT systems. Martina Hasenleitner and Plaetzer [53] reported efficient bacterial inactivation using a tailored LED-based device combined with chlorophyllin or porphyrin-type PS, showing that optimized light delivery significantly enhances PDT outcomes. Food-sector applications, such as the work of Luksiene and Paskeviciute [40], demonstrated that chlorophyllin can achieve rapid inactivation of foodborne pathogens on packaging surfaces, supporting its safety and functional stability under practical conditions. More recently, Zhang *et al*. [54] showed that sodium-copper chlorophyllin induces oxidative membrane damage in *E. coli*, producing strong ROS-mediated photokilling similar to the effects observed in our free chlorophyllin and nanohybrid systems. Within this context, the chlorophyllin–$Cu_3(PO_4)_2$ nanohybrid evaluated in our study exhibited photokilling efficiencies within the established performance range for chlorophyllin-based PDI. This is consistent with reports where immobilized or nanoparticle-bound photosensitizers (e.g., chlorophyllin-chitosan, AuNP-PS hybrids) exhibit improved microbial contact, localized ROS delivery, or enhanced photostability, collectively compensating for reduced solution-phase ROS yields. Thus, the observed antimicrobial outcomes not only align with previous chlorophyllin and hybrid PDT systems but also highlight how nanostructured carriers can modulate the balance between ROS production, PS stability, and cell–PS interactions to achieve functionally relevant bacterial inactivation.

4. Conclusions

This work establishes that chlorophyllin can be effectively immobilized within copper phosphate nanohybrids while retaining its photodynamic antimicrobial properties. The Chlorophyllin-$Cu_3(PO_4)_2$ nanohybrid displayed a characteristic flower-like architecture and achieved complete photokilling of EDR *P. aeruginosa* PAW1 through ROS-mediated disruption of membrane integrity. The absence of dark toxicity and negligible contribution from metal-ion effects confirms that the antimicrobial action is driven primarily by light-activated chlorophyllin. While the results demonstrate strong antibacterial efficacy, this study is limited by the lack of quantitative ROS profiling and cytocompatibility evaluation. Future work should focus on ROS quantification, long-term stability, biofilm inactivation, and safety assessments to validate the suitability of these nanohybrids for practical antimicrobial applications. With further optimization and validation, chlorophyllin-based photodynamic systems may serve as promising candidates for incorporation into disinfection coatings or non-thermal sterilization technologies.

Author Contributions

Conceptualization, U.J.; methodology, U.J., G.G., S.J., S.P., K.P. and G.G.; validation, U.J., G.G., S.J., S.P., K.P. and G.G.; formal analysis, S.S., M.S., S.B. and M.T.; investigation, S.S., M.S., A.J., V.S., S.B. and M.T.; resources, U.J.; data curation, S.S.; writing—original draft preparation, S.S. and U.J.; writing—review and editing, U.J., G.G., S.J., S.P., K.P. and G.G.; supervision, U.J., G.G., S.J., S.P., K.P. and G.G.; project administration, U.J.; funding acquisition, U.J., S.J. and S.P. All authors have read and agreed to the published version of the manuscript.

Institutional Review Board Statement

Not applicable.

Informed Consent Statement

Not applicable.

Data Availability Statement

Data supporting the findings of this study are available upon reasonable request from the corresponding author.

Funding

This research was funded by the Indian Council of Medical Research, grant number [Project ID 2021-10581; Ref: 35/13/2022-NANO/BMS; DT. 2023-01-18].

Acknowledgments

Ms. Manisha Shinde acknowledges the Indian Council of Medical Research for the fellowship and the Department of Microbiology, Savitribai Phule Pune University (SPPU) (Formerly Pune University), Pune, for providing the required facilities. Dr. Umesh Jadhav is thankful to the Indian Council of Medical Research for providing funding to carry out the research (Project ID

2021-10581; Ref: 35/13/2022-NANO/BMS; DT. 2023-01-18). We are thankful to Prof. Anupa Kumbhar and the Department of Chemistry, Savitribai Phule Pune University, Pune, for extending the DLS and zeta potential measurement facility. We are also thankful to the Indian Institute of Science Education and Research (IISER) Pune for providing X-ray diffraction (XRD) analysis.

Conflicts of Interest

The authors declare no conflict of interest. The funders had no role in the design of the study, in the collection, analysis, or interpretation of data, in the writing of the manuscript, or in the decision to publish the results.

References

1. Youf, R.; Müller, M.; Balasini, A.; Thétiot, F.; Müller, M.; Hascoët, A.; Jonas, U.; Schönherr, H.; Lemercier, G.; Montier, T. Antimicrobial photodynamic therapy: Latest developments with a focus on combinatory strategies. *Pharmaceutics* **2021**, *13*, 1995, https://doi.org/10.3390/pharmaceutics13121995.
2. Lu, M.; Li, Y.; Wu, M. Bacteria-specific pro-photosensitizer kills multidrug-resistant *Staphylococcus aureus* and *Pseudomonas aeruginosa*. *Commun. Biol.* 2021, *4*, 1-12, https://doi.org/10.1038/s42003-021-01956-y.
3. Mulani, M.; Kamble, E.; Kumkar, S.; Tawre, M.; Pardesi, K. Emerging strategies to combat ESKAPE pathogens in the era of antimicrobial resistance: A review. *Front. Microbiol.* **2019**, *10*, 539, https://doi.org/10.3389/fmicb.2019.00539.
4. Maisch, T.; Eichner, A.; Späth, A.; Gollmer, A.; König, B.; Regensburger, J.; Bäumler, W. Fast and effective photodynamic inactivation of multiresistant bacteria by cationic riboflavin derivatives. *PloS ONE* **2014**, *9*, e111792, https://doi.org/10.1371/journal.pone.0111792.
5. Tang, W.; Xu, H.; Park, E.; Philbert, M.; Kopelman, R. Encapsulation of methylene blue in polyacrylamide nanoparticle platforms protects its photodynamic effectiveness. *Biochem. Biophys. Res. Commun.* **2008**, *369*, 579-583, https://doi.org/10.1016/j.bbrc.2008.02.066.
6. Jeong, S.; Lee, J.; Im, B.; Park, H.; Na, K. Combined photodynamic and antibiotic therapy for skin disorder via lipase-sensitive liposomes with enhanced antimicrobial performance. *Biomaterials* **2017**, *141*, 243-250, https://doi.org/10.1016/j.biomaterials.2017.07.009.
7. Wijesiri, N.; Ozkaya-Ahmadov, T.; Wang, P.; Zhang, J.; Tang, H.; Yu, X.; Ayres, N.; Zhang, P. Photodynamic inactivation of multidrug-resistant *Staphylococcus aureus* using hybrid photosensitizers based on amphiphilic block copolymer-functionalized gold nanoparticles. *ACS Omega* **2017**, *2*, 5364-5369, https://doi.org/10.1021/acsomega.7b00738.
8. Husain, Q. Nanomaterials immobilized cellulolytic enzymes and their industrial applications: A literature review. *JSM Biochem. Mol. Biol.* **2017**, *4*, 1029, https://doi.org/10.47739/2333-6633/1029.
9. Wang, X.; Shi, J.; Li, Z.; Zhang, S.; Wu, H.; Jiang, Z.; Yang, C.; Tian, C. Facile one-pot preparation of chitosan/calcium pyrophosphate hybrid microflowers. *ACS applied materials & interfaces* **2014**, *6*, 14522-14532, https://doi.org/10.1021/am503787h.
10. Lee, S.W.; Cheon, S.A.; Kim, M.I.; Park, T.J. Organic–inorganic hybrid nanoflowers: types, characteristics, and future prospects. *J. Nanobiotechnol.* **2015**, *13*, 54, https://doi.org/10.1186/s12951-015-0118-0.
11. Wang, L.B.; Wang, Y.C.; He, R.; Zhuang, A.; Wang, X.; Zeng, J.; Hou, J.G. A new nanobiocatalytic system based on allosteric effect with dramatically enhanced enzymatic performance. *J. Am. Chem. Soc.* **2013**, *135*, 1272–1275, https://doi.org/10.1021/ja3120136.
12. Shende, P.; Kasture, P.; Gaud, R. Nanoflowers: the future trend of nanotechnology for multi-applications. *Artif. Cells Nanomed. Biotechnol.* **2018**, *46*, 413-422, https://doi.org/10.1080/21691401.2018.1428812.
13. Hu, R.; Zhang, X.; Zhao, Z.; Zhu, G.; Chen, T.; Fu, T.; Tan, W. DNA nanoflowers for multiplexed cellular imaging and traceable targeted drug delivery. *Angew. Chem. Int. Ed.* **2014**, *53*, 5821-5826, https://doi.org/10.1002/anie.201400323.

14. Zhang, Z.; Zhang, Y.; Song, R.; Wang, M.; Yan, F.; He, L.; Chen, J. Manganese(II) phosphate nanoflowers as electrochemical biosensors for high-sensitivity detection of ractopamine. *Sens. Actuators B Chem.* **2015**, *211*, 310-317, https://doi.org/10.1016/j.snb.2015.01.106.
15. Bhapkar, S.; Kumbhar, N.; Jagtap, S.; Gacche, R.; Barvkar, T.; Sonune, D.; Sonawane, K.; Jadhav, U. Self-assembly of soybean peroxidase nanohybrid for activity enhancement and dye decolorization: Experimental and computational studies. *J. Biomol. Struct. Dyn.* **2022**, *40*, 12739-12749, https://doi.org/10.1080/07391102.2021.1975566.
16. Chandane, P.; Jori, C.; Chaudhari, H.; Bhapkar, S.; Deshmukh, S.; Jadhav, U. Bioleaching of copper from large printed circuit boards for synthesis of organic–inorganic hybrid. *Environ. Sci. Pollut. Res.* **2020**, *27*, 5797-5808, https://doi.org/10.1007/s11356-019-07244-x.
17. Yu, Y.; Fei, X.; Tian, J.; Xu, L.; Wang, X.; Wang, Y. Self-assembled enzyme-inorganic hybrid nanoflowers and their application to enzyme purification. *Colloids Surf. B Biointerfaces* **2015**, *130*, 299–304, https://doi.org/10.1016/j.colsurfb.2015.04.033.
18. Buchovec, I.; Lukseviciute, V.; Marsalka, A.; Reklaitis, I.; Luksiene, Z. Effective photosensitization-based inactivation of Gram-negative food pathogens and molds using the chlorophyllin-chitosan complex. *Photochem. Photobiol. Sci.* **2016**, *15*, 506-516, https://doi.org/10.1039/c5pp00376h.
19. Attaoui, H.; Lbouhmadi, R.; Mouzaki, M.; Mir, Y. Microalgae-derived potassium chlorophyllin as a photosensitizer in antimicrobial photodynamic therapy. *Bioorg. Chem.* **2025**, *164*, 108860, https://doi.org/10.1016/j.bioorg.2025.108860.
20. Somturk, B.; Yilmaz, I.; Altinkaynak, C.; Karatepe, A.; Özdemir, N.; Ocsoy, I. Synthesis of urease hybrid nanoflowers and their enhanced catalytic properties. *Enzyme Microb. Technol.* **2016**, *86*, 134-142, https://doi.org/10.1016/j.enzmictec.2015.09.005.
21. Altinkaynak, C.; Tavlasoglu, S.; Özdemir, N.; Ocsoy, I. A new generation approach in enzyme immobilization: Organic-inorganic hybrid nanoflowers with enhanced catalytic activity and stability. *Enzyme Microb. Technol.* **2016**, *93-94*, 105-112, https://doi.org/10.1016/j.enzmictec.2016.06.011.
22. Heidarizadeh, M.; Doustkhah, E.; Rostamnia, S.; Rezaei, P.; Harzevili, F.; Zeynizadeh, B. Dithiocarbamate-modified magnetic graphene oxide for covalent enzyme immobilization. *Int. J. Biol. Macromol.* **2017**, *101*, 696-702, https://doi.org/10.1016/j.ijbiomac.2017.03.152.
23. Zheng, H.; Cooper, D.; Porebski, P.; Shabalin, I.; Handing, K.; Minor, W. *CheckMyMetal:* A macromolecular metal-binding validation tool. *Struct. Biol.* **2017**, *73*, 223-233, https://doi.org/10.1107/S2059798317001061.
24. Lei, Z.; Gao, C.; Chen, L.; He, Y.; Ma, W.; Lin, Z. Recent advances in biomolecule immobilization based on self-assembly: Organic-inorganic hybrid nanoflowers and metal-organic frameworks. *J. Mater. Chem. B* **2018**, *6*, 1581–1594, https://doi.org/10.1039/C7TB03310A.
25. Fathi, Z.; Doustkhah, E.; Rostamnia, S.; Darvishi, F.; Ghodsi, A.; Ide, Y. Interaction of *Yarrowia lipolytica* lipase with dithiocarbamate-modified magnetic carbon nanoparticles. *Int. J. Biol. Macromol.* **2018**, *117*, 218-224, https://doi.org/10.1016/j.ijbiomac.2018.05.156.
26. Fathi, Z.; Doustkhah, E.; Ebrahimipour, G.; Darvishi, F. Noncovalent immobilization of *Yarrowia lipolytica* lipase on amino acid-functionalized silica nanoparticles. *Biomolecules* **2019**, *9*, 502, https://doi.org/10.3390/biom9090502.
27. Liu, Y.; Ji, X. Organic–inorganic nanoflowers: From design strategy to biomedical applications. *Nanoscale* **2019**, *11*, 17179–17194, https://doi.org/10.1039/C9NR05446D.
28. Ge, J.; Lei, J.; Zare, R. Protein-inorganic hybrid nanoflowers. *Nat. Nanotechnol.* **2012**, *7*, 428–432, https://doi.org/10.1038/nnano.2012.80.
29. Kaur, H.; Bari, N.; Garg, A.; Sinha, S. Protein morphology drives the structure and catalytic activity of bio-inorganic hybrids. *Int. J. Biol. Macromol.* **2021**, *176*, 106-116, https://doi.org/10.1016/j.ijbiomac.2021.01.217.
30. Luo, Y.; Song, F.; Wang, X.; Wang, Y. Pure copper phosphate nanostructures with controlled growth. *CrystEngComm* **2017**, *19*, 2996-3002, https://doi.org/10.1039/C7CE00466D.
31. Jiandong, C.; Jia, S. Organic–inorganic hybrid nanoflowers: A novel host platform for immobilizing biomolecules. *Coord. Chem. Rev.* **2017**, *352*, 249-263, https://doi.org/10.1016/j.ccr.2017.09.008.
32. Escobar, S.; Velasco-Lozano, S.; Lu, C.; Lin, Y.; Mesa, M.; Bernale, C.; Lopez-Gallego, F. Deciphering metal-binding sites in bio-inorganic nanoflowers. *J. Mater. Chem. B* **2017**, *5*, 4478-4486. https://doi.org/10.1039/c6tb03295h.

33. Nakamoto, K. Infrared and Raman Spectra of Inorganic and Coordination Compounds, 6th Edition; Wiley: New York: NY, USA, **2009**.
34. Spiro, T.G.; Li, X. Vibrational Spectroscopy of Porphyrins. In *The Porphyrin Handbook*; Kadish, K.M., Smith, K.M., Guilard, R., Eds.; Academic Press: San Diego, CA, USA, **2000**; Vol. 7, pp 1–51.
35. Devamani, R.; Alagar, M. Synthesis and characterization of copper(II) phosphate nanoparticles. *Elixir Nano Technol.* **2013**, *61*, 16917-16921.
36. Azimi, S.; Behin, J.; Abiri, R.; Rajabi, L.; Derakhshan, A.; Karimnezhad, H. Chlorophyllin-functionalized graphene oxide nanostructures: synthesis and antibacterial activity. *Sci. Adv. Mater.* **2014**, *6*, 771-781, https://doi.org/10.1166/SAM.2014.1767.
37. Nadar, S.; Gawas, S.; Rathod, V. Self-assembled organic–inorganic hybrid glucoamylase nanoflowers. *Int. J. Biol. Macromol.* **2016**, *92*, 660-669, https://doi.org/10.1016/j.ijbiomac.2016.06.071.
38. Yin, Y.; Xiao, Y.; Lin, G.; Xiao, Q.; Lin, Z.; Cai, Z. Enzyme-inorganic hybrid nanoflower reactor with enhanced activity. *J. Mater. Chem. B* **2015**, *3*, 2295-2300, https://doi.org/10.1039/C4TB01697A.
39. Jiang, W.; Wang, X.; Yang, J.; Han, H.; Li, Q.; Tang, J. Lipase-inorganic hybrid nanoflowers for biodiesel synthesis. *J. Colloid Interface Sci.* **2018**, *514*, 102-107, https://doi.org/10.1016/j.jcis.2017.12.025.
40. Luksiene, Z.; Paskeviciute, E. Novel approach to decontaminate food-packaging from pathogens in non-thermal and not chemical way: Chlorophyllin-based photosensitization. *J. Food Eng.* 2011, *106*, 152–158, https://doi.org/10.1016/j.jfoodeng.2011.04.024.
41. Nitzan, Y.; Pechatnikov, I. Photodynamic Inactivation of Microbial Pathogens: Medical and Environmental Applications. In Photodynamic Inactivation of Microbial Pathogens; The Royal Society of Chemistry: London, **2011**; pp. 45-67, https://doi.org/10.1039/9781849733083.
42. Aponiene, K.; Luksiene, Z. Effective LED-based photodynamic inactivation of Gram-negative bacteria. *J. Photochem. Photobiol. B* **2015**, *142*, 257-263, https://doi.org/10.1016/j.jphotobiol.2014.11.011.
43. Wainwright, M.; Maisch, T.; Nonell, S.; Plaetzer, K.; Almeida, A.; Tegos, G.; Hamblin, M. Photoantimicrobials-Are we afraid of the light? *Lancet Infect. Dis.* **2017**, *17*, 49-55, https://doi.org/10.1016/S1473-3099(16)30268-7.
44. Cieplik, F.; Deng, D.; Crielaard, W.; Buchalla, W.; Hellwig, E.; Al-Ahmad, A.; Maisch, T. Antimicrobial photodynamic therapy–what we know and what we don't. *Crit. Rev. Microbiol.* **2018**, *44*, 571-589, https://doi.org/10.1080/1040841X.2018.1467876.
45. Sperandio, F.; Huang, Y.; Hamblin, M. Antimicrobial photodynamic therapy against Gram-negative bacteria. *Recent Pat. Anti-Infect. Drug Discov.* **2013**, *8*, 108-120, https://doi.org/10.2174/1574891X113089990012.
46. Krüger, M.; Richter, P.; Strauch, S.M.; Nasir, A.; Burkovski, A.; Antunes, C.A.; Meißgeier, T.; Schlücker, E.; Schwab, S.; Lebert, M. What an Escherichia coli mutant can teach us about the antibacterial effect of chlorophyllin. *Microorganisms* **2019**, *7*, 59, https://doi.org/10.3390/microorganisms7020059.
47. Cieplik, F.; Steinwachs, V.-S.; Muehler, D.; Hiller, K.-A.; Thurnheer, T.; Belibasakis, G.N.; Buchalla, W.; Maisch, T. Phenalen-1-one-mediated antimicrobial photodynamic therapy: antimicrobial efficacy in a periodontal biofilm model and flow cytometric evaluation of cytoplasmic membrane damage. *Front. Microbiol.* **2018**, *9*, 688, https://doi.org/10.3389/fmicb.2018.00688.
48. Guo, Z.; Zhou, X.; Hou, C.; Ding, Z.; Wen, C.; Zhang, L.-J.; Jiang, B.-P.; Shen, X.-C. A chloroplast-inspired nanoplatform for targeting cancer and synergistic photodynamic/photothermal therapy. *Biomater. Sci.* **2019**, *7*, 3886-3897, https://doi.org/10.1039/C9BM00762H.
49. Lihuan, D.; Jingcun, Z.; Ning, J.; Guozeng, W.; Yiwei, C.; Wei, L.; Jing, Q.; Yuanfang, Z.; Gang, C. Photodynamic therapy with the novel photosensitizer chlorophyllin f induces apoptosis and autophagy in human bladder cancer cells. *Lasers Surg. Med.* **2014**, *46*, 319-334, https://doi.org/10.1002/lsm.22225.
50. Arifianto, D.; Astuti, S.D.; Medyaz, S.R.; Lestari, S.B.; Samian, S.; Nurdin, D.Z.I.; Hariyani, D.A.; Susilo, Y.; Syahrom, A. Comparison of the antimicrobial reduction effect of photodynamic inactivation with the addition of chlorophyll and curcumin photosensitizer in Aggregatibacter actinomycetemcomitans and Enterococcus faecalis. *F1000Research* **2025**, *12*, 142, https://doi.org/10.12688/f1000research.128483.1.
51. Wimmer, A.; Jernej, L.; Liu, J.; Fefer, M.; Plaetzer, K. Chlorophyllin-based photodynamic inactivation against *Candidozyma auris*. *Photochem. Photobiol. Sci.* **2025**, *24*, 1393-1405, https://doi.org/10.1007/s43630-025-00768-x.
52. Pohland, S.; Vourvoutsiotou, J.; Brandtner, L.; Geißler, D.; Wiesmeth, S.; Scudlo, V.; Richter, P.; Burkovski, A.; Lebert, M. Chlorophyllin-Mediated Photodynamic Inactivation: Dosage and Time

Dependency in the Inhibition of Bacillus subtilis. *Microorganisms* **2025**, *13*, 1189, https://doi.org/10.3390/microorganisms13061189.
53. Hasenleitner, M.; Plaetzer, K. Photodynamic inactivation using LED-based illumination devices. *Antibiotics* **2020**, *9*, 13, https://doi.org/10.3390/antibiotics9010013.
54. Zhang, Z.; Qin, J.; Wang, Z.; Chen, F.; Liao, X.; Hu, X. Sodium copper chlorophyll-mediated photodynamic inactivation of *Escherichia coli*. *Food Res. Int.* **2022**, *157*, 111472, https://doi.org/10.1016/j.foodres.2022.111472.

Publisher's Note & Disclaimer